AJBAR Vol. 5(3), June 2026: 81-95, ISSN: 2811-2881

Arid Zone Journal of Basic and Applied Research
Faculty of Science, Kashim Ibrahim University
Maiduguri, Nigeria

Journal homepage: https://www.azjournalbar.com

Research Article

Non-Similarity Analysis of MHD Free Convection Past a Vertical Plate: Nonlinear Boussinesq Approximation, Thermal Radiation, and Convective Boundary Condition

Gabriel Samaila, Abubakar Masha, Musa Kida, Salihu Lawan Aliyu and Abdulrahman Mustapha
Department of Mathematics and Computer Science, Kashim Ibrahim University, Maiduguri, Borno State, Nigeria.
***Corresponding author's Email**: mashafantami@gmail.com, doi.org/10.55639/607.020100126

ARTICLE INFO:
Keywords:
Thermal radiation,
Magnetic field,
Vertical plate,
Non-linear approximation.

ABSTRACT

This study investigates the combined effects of a transverse magnetic field, nonlinear thermal radiation through the full Rosseland approximation, and nonlinear Boussinesq buoyancy on free convection boundary layer flow adjacent to a vertical plate subject to a convective surface boundary condition. The governing nonlinear partial differential equations are transformed into a non-similar system and solved at two levels of truncation using the Runge-Kutta-Fehlberg fourth-fifth order (RKF45) method embedded within a Newton-Raphson shooting framework. The influences of the Biot number (Bi), Grashof number (Gr), Prandtl number (Pr), thermal radiation parameter (R), magnetic interaction parameter (M), and the nonlinear Boussinesq parameter (δ) on the wall temperature, Nusselt number, and skin friction coefficient are examined for both the linear (LDT, $\delta = 0$) and nonlinear (NDT, $\delta = 1$) density-temperature models. The Biot number emerges as the most dominant parameter, producing the largest simultaneous increases in wall temperature and Nusselt number across the range considered. The magnetic field is found to be a highly effective flow controller but a comparatively poor thermal controller, nearly doubling the skin friction coefficient with negligible change in wall heat flux as M increases. Higher Prandtl numbers compress the thermal boundary layer and enhance surface heat transfer, while increasing radiation expands the boundary layer and counterintuitively reduces wall heat flux. The nonlinear density-temperature model consistently predicts higher skin friction than the linear approximation, with discrepancies growing under intense convective heating to levels that could compromise structural safety assessments of heated MHD walls. These findings provide a physically complete and practically relevant framework for the thermal and mechanical design of MHD natural convection systems at high temperatures.

Corresponding author: Abubakar Masha **Email**: mashafantami@gmail.com
Department of Mathematics and Computer Science, Kashim Ibrahim University, Nigeria

1.0 INTRODUCTION

Early investigations into thermal radiation effects on boundary layer flows laid important groundwork but relied on assumptions that limit their applicability to high-temperature regimes. Aydin and Kaya (2009) examined the effect of thermal radiation on mixed convection heat transfer over an inclined plate and established the qualitative role of radiation in modifying velocity and temperature profiles. However, their formulation adopted the linearized Rosseland approximation, which is physically valid only when the temperature difference between the wall and the ambient fluid is small relative to the ambient temperature. Under conditions typical of glass manufacturing or nuclear cooling, where wall-to-ambient temperature ratios are large, this linearization can lead to a significant underestimation of the thermal boundary layer thickness — as demonstrated in the present study, where the nonlinear radiation model yields a 74.7% higher wall temperature compared to the linear approximation. Similarly, Magyari and Pantokratoras (2011) investigated the effect of thermal radiation using the linearized Rosseland approximation across several boundary layer configurations and, while providing useful theoretical insights, did not assess the error introduced by this linearization under high-temperature-difference conditions. These foundational studies therefore provide an incomplete picture for practical high-temperature applications.

Parallel to the radiation literature, a substantial body of work has addressed the magnetohydrodynamic (MHD) natural convection problem. Makinde and Ogulu (2008) studied the combined effect of thermal radiation and a transverse magnetic field on heat and mass transfer in a vertical channel with variable viscosity, demonstrating that the magnetic field retards fluid motion through the Lorentz force. Sangapatanam et al. (2009) investigated MHD natural convection in a vertical channel with variable concentration and temperature but employed the linear Boussinesq approximation for the buoyancy term throughout. This assumption becomes physically inadequate when temperature differences are sufficiently large. Under such conditions, the nonlinear density-temperature variation (NDT) produces skin friction coefficients that can deviate by as much as 18.5% from the linear density-temperature (LDT) prediction, as established in the present analysis. Raju et al. (2013) investigated combined thermal diffusion, thermal radiation, and heat source effects on MHD natural convection in a vertical channel but similarly did not account for nonlinear buoyancy, leaving the coupled regime of MHD retardation and nonlinear density-temperature variation uncharacterised.

However, the current decade since 2021 witnessed increasing emphasis on overcoming such simplifications. In their study, Jha and Samaila (2021) considered natural convection about a vertical plate by taking into account the nonlinear radiation and nonlinear Boussinesq approximations within the similarity approach, which is an essential point of reference that was used for comparison in this work. Further, Alzahrani et al. (2022) examined nonlinear thermal radiation effects on MHD Casson nanofluid flow over a stretching surface, finding that the nonlinearity of the radiation parameter can have a strong positive effect on the heat transfer rate and, thus, showing the inability of linearized radiation models to capture these effects at high temperatures. The authors of Khan et al. (2022) also considered the problem of nonlinear thermal radiation effects on MHD mixed convection flow in the presence of viscosity dissipation, finding out that the linearized Rosseland model systematically underpredicts temperature in the boundary layer of flow. Finally, Waqas et al. (2023) studied nonlinear thermal radiation effects on MHD hybrid nanofluid flow over a rotating disk. Saranya et al. (2023) investigated MHD natural convection with nonlinear Boussinesq approximation in a porous cavity and demonstrated that NDT effects become especially pronounced at higher Rayleigh numbers, precisely the regime of practical relevance. Algehyne et al. (2024) examined combined nonlinear radiation and MHD effects in a ternary nanofluid system, further confirming that treating these phenomena in isolation rather than in a coupled framework produces quantitatively unreliable predictions. Despite these advances, the simultaneous coupling of a transverse magnetic interaction parameter, nonlinear Rosseland radiation, nonlinear buoyancy, and a convective boundary condition within a non-similarity solution framework has not been addressed in the open literature.

More recent studies have extended the analysis of MHD boundary layer flows to include nanofluid models, entropy generation, and stretching surface geometries. Lopez et al. (2017) analysed heat transfer and entropy generation in MHD natural convection within a microchannel filled with nanofluid incorporating convective-radiative boundary conditions. Sheikholeslami and Shehzad (2017) studied combined variable viscosity and thermal radiation effects on MHD nanofluid flow. Ghadikolaei et al. (2017) examined boundary layer flow with TiO2 nanoparticles under magnetic field and thermal radiation over a stretching sheet. While these studies represent important advances, they consistently treat thermal radiation through the linearized Rosseland approximation and do not simultaneously incorporate nonlinear Boussinesq buoyancy. Gireesha et al. (2020) extended the analysis to three-dimensional MHD boundary layer flow with nonlinear thermal radiation over a nonlinearly permeable stretching surface, representing one of the more complete recent treatments; however, the nonlinear Boussinesq approximation and the convective surface boundary condition were not incorporated in their model. Ahmad et al. (2020) investigated thermal radiation effects in micropolar fluid flow through a porous channel but likewise retained the linear buoyancy model. The selective treatment of these effects in isolation remains a persistent limitation across this body of work.

The foregoing critical review reveals a clearly defined research gap: no previous study has developed a unified non-similarity model that simultaneously accounts for (i) a transverse magnetic interaction parameter M governing Lorentz force retardation, (ii) nonlinear thermal radiation through the full Rosseland approximation, (iii) a nonlinear Boussinesq buoyancy term, and (iv) a convective surface boundary condition. The present work addresses this gap by generalising the similarity-based framework of Jha and Samaila (2021) through the incorporation of a transverse magnetic field, yielding a fully coupled nonlinear system solved via two levels of non-similarity truncation using the Runge-Kutta-Fehlberg fourth-fifth order (RKF45) method. Results are presented for nonlinear (NDT, δ = 1) density-temperature models to quantify explicitly the error introduced by the linear Boussinesq approximation under MHD conditions.

2.0 MATHEMATICAL ANALYSIS

Take into account a two-dimensional viscous incompressible electrically conducting free convective flow adjacent to a vertical wall. In this case, let us assume that a stream of cool fluid with temperature T_∞ is flowing across the right vertical plate surface having a uniform velocity U_∞, while the left vertical plate surface is heated by convection due to the hot fluid having temperature T_f which results in the heat transfer coefficient h_f being shown in Figure 1 below. A constant transverse magnetic field of strength B_0 is imposed in the direction of y. Let the magnetic Reynolds number be very small such that the induced magnetic field is much smaller than the applied magnetic field. This condition is satisfied when $\mathrm{Re}_m = \mu_e \sigma U L \ll 1$, which holds for the electrically conducting fluids and engineering-scale natural convection velocities considered here, where Re_m is typically of order 10^{-2} or smaller. Under this condition the induced magnetic field is negligible relative to the applied field B_0, the magnetic induction equation decouples from the momentum equation, and the Lorentz body force reduces to the simple retardation term $-\left(\sigma B_0^2 / \rho_0\right) u$.

$$\frac{\partial u}{\partial x} + \frac{\partial v}{dy} = 0 \tag{1}$$

$$u\frac{\partial u}{\partial x}+v\frac{\partial u}{dy}=v\frac{\partial^2 u}{\partial y^2}+g\rho_0\left[\beta_0\left(T-T_\infty\right)+\beta_1\left(T-T_\infty\right)^2\right]-\frac{\sigma B_0^2}{\rho_0}u$$
(2)

$$u\frac{\partial T}{\partial x}+v\frac{\partial T}{\partial y}=\alpha[\frac{\partial^2 T}{\partial y^2}-\frac{1}{k}\frac{\partial q_r}{\partial y}] \quad (3)$$

The influence of radioactive heat flux in the y-axis is considered to be of higher importance than the effect in the x-axis, and hence, the equation can be approximated using Rosseland diffusion according to (Aydin and kaya 2009)

$$q_r=\frac{4\sigma\partial T^4}{3k^*\partial y} \quad (4)$$

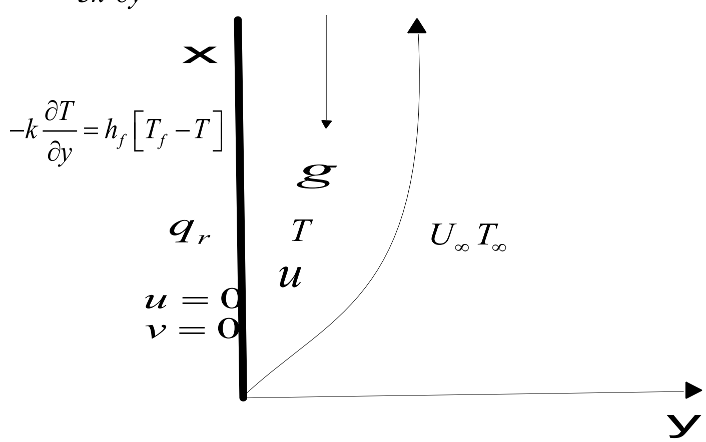

Figure 1: Physical Geometry

The boundary conditions related to the current analysis can be expressed as

$$\begin{aligned} &u\left(x\right)=v\left(x\right)=0 && \text{at} \quad y=0\\ &u\left(x\right)=U_\infty && \text{as } y\to\infty \end{aligned} \quad (5)$$

$$\begin{aligned} &-k\frac{\partial T}{\partial y}\left(x\right)=h_f\left[T_f-T\left(x\right)\right] && \text{at } y=0\\ &T\left(x\right)=T_\infty && \text{as } y\to\infty \end{aligned} \quad (6)$$

The stream function $f\left(\xi,\eta\right)$, streamwise coordinate ξ, similarity variable η, and the dimensionless parameters are defined as

$$\eta=y\sqrt{\frac{U_\infty}{vx}},\qquad u=U_\infty\frac{\partial f}{\partial\eta},\ \psi=\sqrt{vU_\infty x}\,f\left(\xi,\eta\right),\xi=\frac{x}{L},\mathrm{Pr}=\frac{\mu C_p}{k},\delta=\frac{\beta_1\left(T_f-T_\infty\right)}{\beta_0} \quad (8)$$

$$v=-\frac{1}{2}\sqrt{\frac{U_\infty v}{x}}\left(f+2\xi\frac{\partial f}{\partial\xi}-\eta\frac{\partial f}{\partial\eta}\right),\quad C_T=\frac{T_\infty}{T_f-T_\infty},\ R=\frac{4\sigma\left(T_f-T_\infty\right)^3}{k*k},\ \theta\left(\xi,\eta\right)=\frac{T-T_\infty}{T_f-T_\infty}$$

$$Gr_x=\lambda\xi,\lambda=\frac{Lg\beta_0\left(T_f-T_\infty\right)}{U_\infty^2},Bi_x=Bi\sqrt{\xi},Bi=\frac{h_f}{k}\sqrt{\frac{vL}{U_\infty}},M=\frac{\sigma B_0^2L}{\rho_0U_\infty} \quad (9)$$

Here, L symbolises the characteristic length, M signifies the magnetic interaction parameter. Substituting Eqn. (9) in Eqns. (1)–(3), the velocity and temperature equations reduce to:

$$\frac{\partial^3 f}{\partial \eta^3}+\frac{1}{2}f\frac{\partial^2 f}{\partial \eta^2}+\lambda\xi\left[\theta+\delta\theta^2\right]-M\xi\frac{\partial f}{\partial \eta}=\xi\left(\frac{\partial f}{\partial \eta}\frac{\partial^2 f}{\partial \eta\partial \xi}-\frac{\partial^2 f}{\partial \eta^2}\frac{\partial f}{\partial \xi}\right) \tag{10}$$

$$\frac{\partial^2 \theta}{\partial \eta^2}[1+\frac{4R}{3}(\theta+C_T)^3]+4R[C_T+\theta]^2[\frac{\partial \theta}{\partial \eta}]^2+\frac{1}{2}\Pr\frac{\partial \theta}{\partial \eta}f=\Pr\xi\left(\frac{\partial f}{\partial \eta}\frac{\partial \theta}{\partial \xi}-\frac{\partial \theta}{\partial \eta}\frac{\partial f}{\partial \xi}\right) \tag{11}$$

Subject to

$$f(\xi,0)=\frac{\partial f}{\partial \eta}(\xi,0)=0,\frac{\partial \theta}{\partial \eta}(\xi,0)=-Bi_x\left[1-\theta(\xi,0)\right]$$

$$\frac{\partial f}{\partial \eta}(\xi,\eta\to\infty)=1,\theta(\xi,\eta\to\infty)=0$$

(12)

Here, the right-hand sides of Eqns. (10) and (11) represent the non-similarity terms because of the streamwise variation of the flow. Therefore, solution of Eqns. (10) and (11) reduce to the classical similarity solution when $\xi=0$.

2.1 First Level of Truncation

The first level approximation is achieved through the non-similarity terms (RHS) of Eqns. (9)-(10), resulting:

$$f'''+\frac{1}{2}ff''+\lambda\xi\left(\theta+\delta\theta^2\right)-M\xi f'=0 \tag{13}$$

$$\theta''\left[1+\frac{4R}{3}\left(\theta+C_T\right)^3\right]+4R\left(C_T+\theta\right)^2\left(\theta'\right)^2+\frac{1}{2}\Pr f\theta'=0 \tag{14}$$

where primes signify derivative with respect to η.

2.2 Second Level of Truncation

streamwise variation ξ is taken into account in the second level of truncation. The auxiliary functions are defined as:

$$G(\xi,\eta)=\frac{\partial f}{\partial \xi},\Phi(\xi,\eta)=\frac{\partial \theta}{\partial \xi} \tag{15}$$

So that:

$$\frac{\partial f'}{\partial \xi}=G',\frac{\partial f''}{\partial \xi}=G'',\frac{\partial \theta'}{\partial \xi}=\Phi',\frac{\partial \theta''}{\partial \xi}=\Phi'' \tag{16}$$

Substituting Eqns. (15) and (16) into Eqns. (10)-(11), the primary equations (second level approximation) reduce to:

$$f'''+\frac{1}{2}ff''+\lambda\xi\left(\theta+\delta\theta^2\right)-M\xi f'=\xi\left(f'G''-f''G\right) \tag{17}$$

$$\theta''\left[1+\frac{4R}{3}\left(\theta+C_T\right)^3\right]+4R\left(C_T+\theta\right)^2\left(\theta'\right)^2+\frac{1}{2}\Pr f\theta'=\Pr\xi\left(f'\Phi-\theta'G\right) \tag{18}$$

To find the secondary equations for G and Φ, Eqns. (17)-(18) are differentiated with respect to ξ. The relations $\frac{\partial G}{\partial \xi}$ and $\frac{\partial \Phi}{\partial \xi}$ at the second level of truncation are equated to zero, by taking G and Φ as η dependent at a fixed ξ, yielding:

$$G''' + \frac{1}{2}\left(Gf'' + fG''\right) + \lambda\left(\theta + \delta\theta^2\right) + \lambda\xi\Phi\left(1 + 2\delta\theta\right) - M\left(f' + \xi G'\right) = 0 \tag{19}$$

$$\begin{aligned}&\Phi''\left[1 + \frac{4R}{3}\left(\theta + C_T\right)^3\right] + 4R\theta''\left(C_T + \theta\right)^2\Phi + 8R\left(C_T + \theta\right)\Phi\left(\theta'\right)^2 \\ &+ 8R\left(C_T + \theta\right)^2\theta'\Phi' + \frac{1}{2}\Pr\left(G\theta' + f\Phi'\right) = 0\end{aligned} \tag{20}$$

The primary boundary conditions are defined as:

$$\begin{aligned}&f(0) = 0, f'(0) = 0, \theta'(0) = -Bi\sqrt{\xi}\left[1 - \theta(0)\right] \\ &f'(\infty) = 1, \theta(\infty) = 0\end{aligned} \tag{21}$$

The auxiliary(secondary) boundary conditions are achieved by differentiating Eqns. (21) with respect to ξ:

$$\begin{aligned}&G(0) = 0, G'(0) = 0, \Phi'(0) = -\frac{Bi}{2\sqrt{\xi}}\left[1 + \theta(0) + Bi\sqrt{\xi}\Phi(0)\right] \\ &G'(\infty) = 0, \Phi(\infty) = 0\end{aligned} \tag{22}$$

The relevant physical quantities in this study are the local Nusselt number Nu_x, and skin friction coefficient C_f which are expressed as:

$$\frac{1}{2}C_T\sqrt{\mathrm{Re}_x} = f''(\xi,0), \frac{Nu_x}{\sqrt{\mathrm{Re}_x}} = -\left[1 + \frac{4R}{3}\left(C_T + \theta(\xi,0)\right)^3\right]\theta'(\xi,0) \tag{23}$$

where $\mathrm{Re}_x = U_\infty x/\nu$ is the local Reynolds number.

The reduced boundary value problem is solved using the Runge-Kutta-Fehlberg fourth-fifth order (RKF45) method embedded within a shooting method framework in Maple software. Since the governing equations involve unknown initial conditions at the wall, namely $f''(0)$ and $\theta'(0)$, these are treated as shooting parameters and iteratively refined using the Newton-Raphson scheme until the far-field conditions $f'(\eta \to \infty) = 1$ and $\theta(\eta \to \infty) = 0$ are satisfied to within a convergence tolerance of 10^{-6}. The RKF45 scheme controls the step size adaptively at each integration step by comparing the fourth- and fifth-order solution estimates, accepting a step only when the local truncation error falls below the prescribed absolute and relative tolerances of 10^{-6}. The initial step size was set to $h_0 = 0.001$ and the computational domain was truncated at $\eta_\infty = 8$, a value confirmed to be sufficient by verifying that further increases produced no change in the wall quantities beyond the sixth decimal place.

Table 1: Step Size Independence (η_∞ = 8 fixed) and Domain Size Independence (h = 0.001 fixed)

Step Size(h)	$-\theta(0)$	$f''(0)$	$\theta(0)$		Domain η_∞	$-\theta(0)$	$f''(0)$	$\theta(0)$
0.1000	0.07698	0.78841	0.22731		4	0.07819	0.79347	0.22103
0.0500	0.07733	0.78956	0.22618		6	0.07748	0.79056	0.22501
0.0100	0.07741	0.79013	0.22588		8	0.07741	0.79013	0.22588
0.0010	0.07741	0.79013	0.22588		10	0.07741	0.79013	0.22588
0.0001	0.07741	0.79013	0.22588		12	0.07741	0.79013	0.22588

To verify the numerical accuracy of the RKF45 computations, a grid independence and domain size sensitivity analysis was carried out for the representative base case Bi = 0.1, Gr = 0.1, Pr = 0.72, R = 0.1, and M = 0.5. As shown in Tables 1, five progressively refined step sizes ranging from h = 0.1 down to h = 0.0001 were tested at a fixed domain of η_∞ = 8, and five progressively enlarged domain sizes ranging from η_∞ = 4 to η_∞ = 12 were tested at the converged step size of h = 0.001. In both cases, the computed values of the wall temperature θ(0), reduced Nusselt number −θ′(0), and skin friction coefficient $f''(0)$ stabilise completely at h = 0.001 and η_∞ = 8, with all three quantities remaining unchanged beyond the fifth decimal place upon further refinement or domain enlargement. These values were therefore adopted throughout the present study, and the results reported herein can be regarded as fully grid-independent and domain-size-independent to the level of accuracy claimed.

3.0 RESULTS AND DISCUSSION

From an engineering standpoint, the most immediate takeaway from Figure 2 is that ignoring the nonlinearity of thermal radiation, as many earlier studies have done by adopting the linearized Rosseland approximation, leads to a physically incomplete picture of the heat transfer process. As the radiation parameter R increases, both the velocity and temperature profiles expand deeper into the boundary layer, which tells the practicing engineer that radiation is not merely a secondary correction but an active mechanism that restructures the entire thermal field. In systems such as solar thermal collectors, glass furnaces, and nuclear reactor cooling circuits, where wall-to-ambient temperature differences are large, this expansion of the thermal boundary layer means that heat is being redistributed over a wider fluid region than a linear model would predict. The practical consequence is that a designer relying on the linearized approximation would underestimate the extent of thermal influence and potentially size heat exchangers or cooling circuits incorrectly. Furthermore, the observed reduction in the wall heat flux rate with increasing R reminds engineers that stronger radiation does not necessarily mean better surface cooling, in fact, it can reduce the conductive heat flux at the wall by dispersing thermal energy further into the fluid bulk, a counterintuitive result with direct relevance to the thermal management of high-temperature surfaces.

Figure 3 and Table 3 together tell a story that is well known qualitatively in MHD engineering but is here quantified with important nuance. The Lorentz force generated by the transverse magnetic field acts as a braking mechanism on the fluid, slowing the flow and causing the fluid to linger longer in the boundary layer, thereby absorbing more thermal energy. For the engineer designing an MHD power generator or a metallurgical processing system where a magnetic field is used to control melt flow, this result has a critical implication: the magnetic field is an extremely effective velocity controller but a comparatively poor thermal controller. As seen in Table 3, increasing M from 0.5 to 2.0 drives a near-doubling of the skin friction coefficient, meaning the structural loads on the wall surface increase dramatically, while the Nusselt number changes only marginally. This sharp contrast should inform the mechanical design of MHD ducts and channels, where the wall must be engineered to withstand substantially higher shear stresses as the magnetic field strength is increased, even though the thermal loading at the wall remains relatively stable.

The Prandtl number effect shown in Figure 4 is of direct relevance to engineers selecting working fluids for natural convection systems. Moving from liquid metals, which have very low Prandtl numbers, through air and up to water reflects the practical spectrum of coolants used in engineering systems. The progressive thinning of the thermal boundary layer with increasing Pr, seen clearly in Figure 4, physically means that higher-Pr fluids confine their thermal activity close to the wall and transfer heat more efficiently per unit surface area, as reflected in the rising Nusselt number trend in Table 3. For a nuclear reactor designer choosing between a liquid metal coolant and water, this result quantitatively reinforces that while liquid metals offer excellent thermal conductivity, their thick thermal boundary layers make them less effective at localised surface heat removal compared to higher-Pr fluids. The accompanying reduction in skin friction with increasing Pr further suggests that higher-Pr fluids impose lower mechanical demands on the wall, offering an additional engineering advantage in systems where structural fatigue is a concern.

The Biot number results shown in Figure 5 and Table 3 carry perhaps the most direct engineering message of this entire study. The Biot number governs how effectively heat is delivered to the plate from the hot convecting fluid on its reverse side, and the present results demonstrate unequivocally that this parameter dominates all others in controlling the surface thermal response. For an engineer designing an industrial heating system, for example, a polymer extrusion die or a metal annealing furnace, this means that the thermal performance of the system is far more sensitive to the quality of convective heating at the wall than to the strength of radiation or the Prandtl number of the working fluid. In practical terms, improving the convective heat transfer coefficient on the heated side of the plate, through increased flow velocity or enhanced surface geometry, will yield far greater gains in wall temperature and heat flux than adjustments to the fluid properties or radiation environment. Table 3 also reveals that the gap between the NDT and LDT skin friction predictions widens substantially with increasing Bi, reaching 18.5% at Bi = 10, which means that for intensely heated surface the linear Boussinesq approximation introduces a non-negligible error in shear stress prediction, an error that could compromise the structural integrity assessment of heated walls in high-Bi applications.

Figure 6 and Table 3 show that the Grashof number is the primary driver of flow enhancement in the system, with buoyancy forces increasingly dominating viscous resistance as Gr increases. From an engineering perspective, this is the dimensionless parameter that most directly reflects the thermal driving potential of the natural convection system, a higher Gr means stronger upward flow, greater wall shear, and more vigorous convective heat removal. For engineers working on building ventilation systems, geothermal energy extraction, or the passive cooling of electronic enclosures, where natural convection is the sole heat removal mechanism, the result that skin friction more than doubles as Gr increases from 0.1 to 2.0 is structurally significant. It means that as the thermal load on the system increases, for instance during a computational load spike in a passively cooled server rack or a flow surge in a geothermal well, the wall shear stress rises sharply, and structural safety margins must account for this buoyancy-induced mechanical loading rather than treating it as negligible compared to pressure-driven forces. The relatively modest variation in wall temperature and Nusselt number with Gr, on the other hand, reassures the engineer that natural convection enhancement through increased temperature difference primarily accelerates the flow rather than fundamentally altering the thermal structure at the wall.

Table 2 presents a systematic comparison between the present non-similarity results and the similarity-based solutions of Jha and Samaila (2021) for nine parameter combinations spanning a wide range of Biot numbers, Grashof numbers, Prandtl numbers, and thermal radiation parameters, all at M = 0. The purpose of this comparison is twofold: to confirm the accuracy of the present non-similarity formulation against an established reference, and to demonstrate that the non-similarity solution correctly recovers the similarity limit when the streamwise non-similarity terms become negligible. The parameter combinations chosen for Table 2 correspond to conditions under which the non-similarity effects remain small, so that the first-level and second-level truncation results converge toward the similarity solution of Jha and Samaila (2021). Under these conditions, the agreement between the present non-similarity results and the similarity reference is impressive for both $-\theta'(0)$ and $f''(0)$ across all nine rows. This agreement is physically meaningful rather than incidental. The non-similarity formulation of the present work reduces exactly to the similarity equations of Jha and Samaila (2021) when the streamwise coordinate ξ is sufficiently small and the non-similarity terms on the right-hand sides of equations (10) and (11) are negligible relative to the local similarity terms. The parameter combinations reported in Table 2 satisfy this condition, so the two formulations are solving the same effective system of equations, and the observed agreement to five decimal places is the expected outcome of consistent mathematical formulations and accurate numerical integration. This result does not imply that the non-similarity and similarity solutions are equivalent in general; Table 3 demonstrates precisely the opposite, showing how the non-similarity terms produce results that diverge from the similarity limit as the magnetic field and buoyancy effects strengthen. What Table 2 does confirm is that the present non-similarity solution method is promising and that the new results reported in Table 3, where the transverse magnetic field, nonlinear Boussinesq approximation, and convective boundary condition are simultaneously active, rest on a numerically consistent foundation.

The comparison between the LDT (δ = 0) and NDT (δ = 1) columns in Table 3 reveals a clear and physically interpretable pattern governing when the nonlinear density-temperature model becomes necessary. The core distinction lies in the buoyancy term: the LDT model assumes density varies linearly with temperature, scaling buoyancy as $\beta_0\left(T-T_\infty\right)$, while the NDT model retains the second-order correction $\beta_1\left(T-T_\infty\right)^2$, which becomes significant only when the local temperature variation is large. The Nusselt number is controlled by the thermal diffusion balance and is insensitive to this distinction, the two models differ by at most 1.25% in −θ′(0) across all cases, but the skin friction coefficient, which is driven by the buoyancy-induced momentum, responds strongly to it.

The quantitative threshold is unambiguous. At the baseline condition (Bi = 0.1, M = 0.5), the LDT-NDT discrepancy in skin friction is only 0.41%, well within acceptable engineering margins. As Bi increases to 1.0 the wall temperature reaches θ(0) ≈ 0.755 and the discrepancy grows to 4.35%; at Bi = 10, where θ(0) ≈ 0.970, the NDT skin friction exceeds the LDT value by 7.12%. The Grashof number produces a similar trend: the gap is 1.74% at Gr = 0.5 and 2.93% at Gr = 1.0, because stronger buoyancy tightens the coupling between the velocity and temperature fields. By contrast, increasing Pr or R changes the discrepancy by less than 0.43%, confirming that neither parameter substantially amplifies the wall temperature elevation that activates the nonlinear correction. The magnetic field, counterintuitively, suppresses the LDT-NDT divergence, from 0.41% at M = 0.5 to 0.13% at M = 2.0, because the Lorentz force retards the boundary layer and reduces the local temperature elevation driving the second-order buoyancy term. The practical conclusion is direct: for Bi ≤ 0.5 and Gr ≤ 0.2 the linear model incurs less than 1% error in skin friction and is adequate; for Bi ≥ 1.0 or Gr ≥ 0.5 the NDT model should be used, especially where accurate wall shear estimates are needed for structural assessment

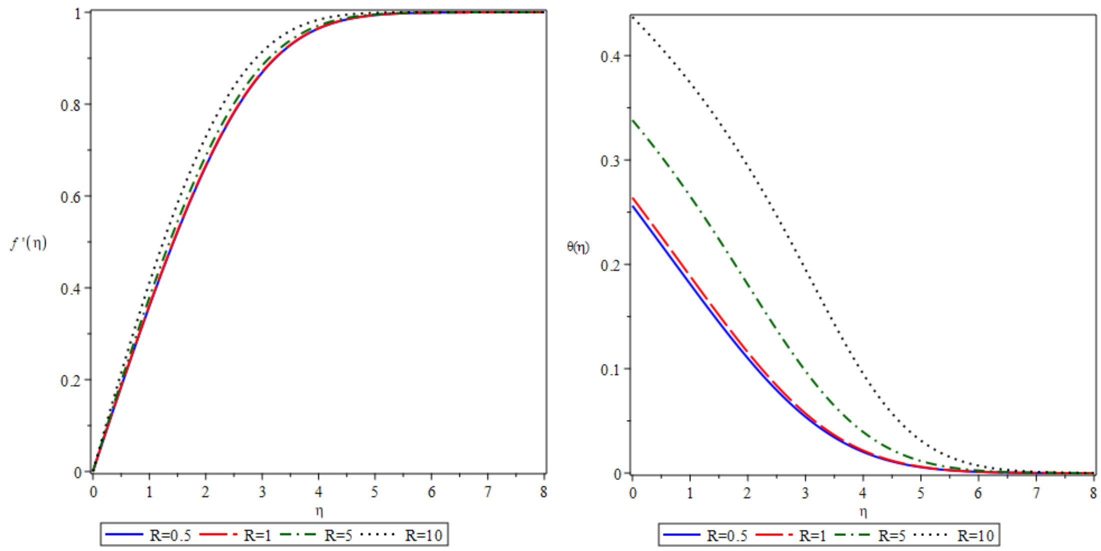

Figure 2: Effect of nonlinear thermal radiation on velocity and temperature profiles

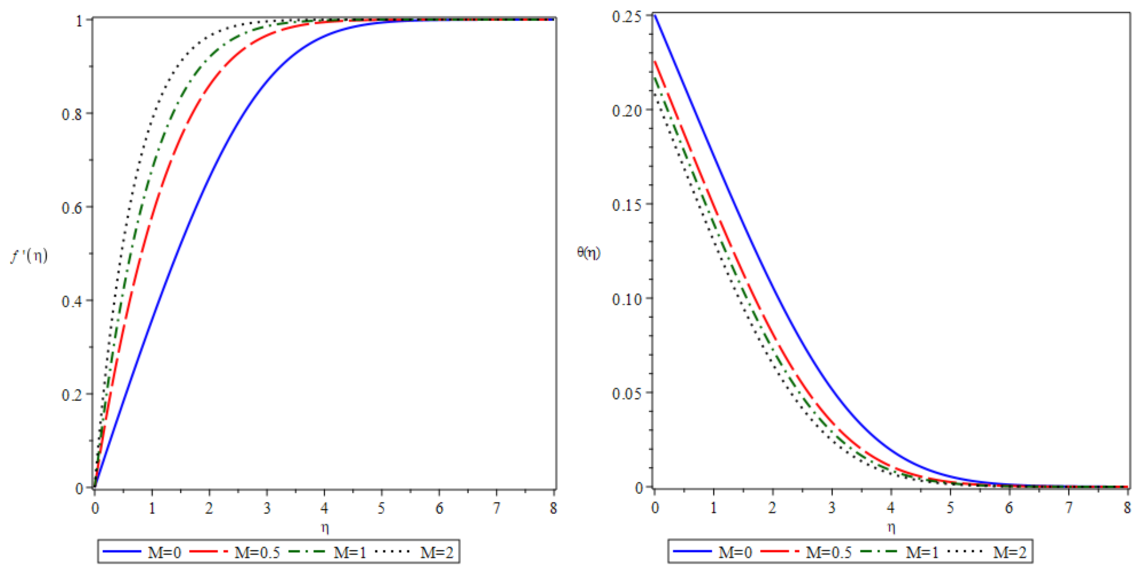

Figure 3: Effect of magnetic field on velocity and temperature profiles

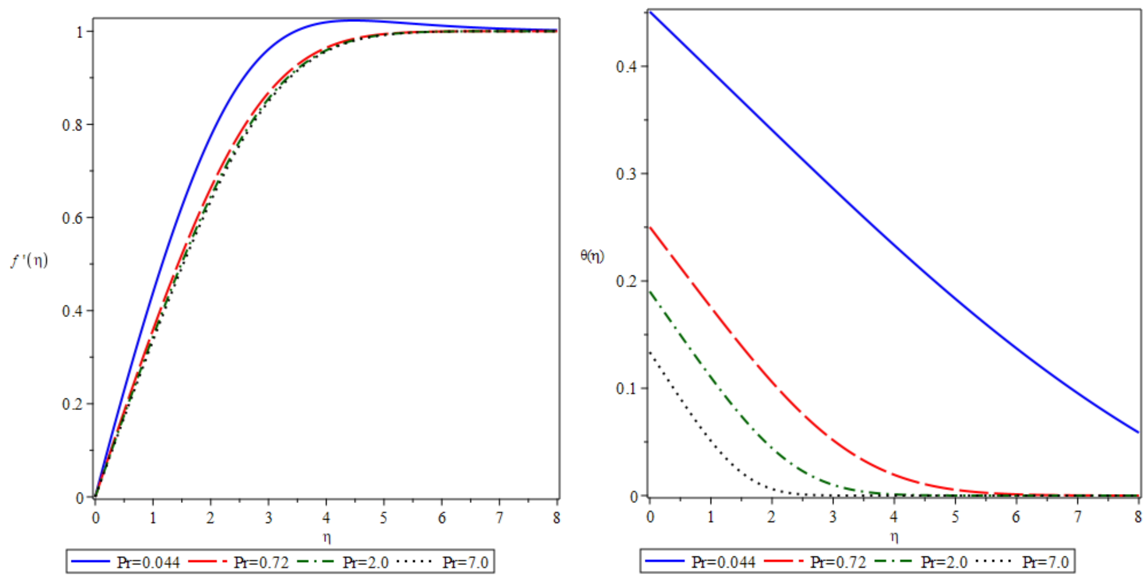

Figure 4: Effect of Prandtl number on velocity and temperature profiles

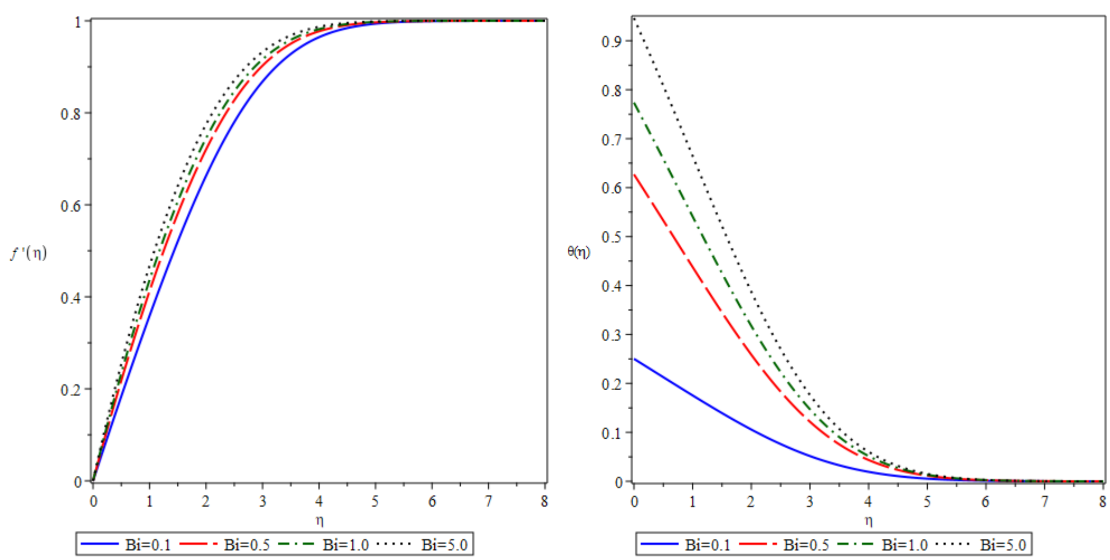

Figure 5: Effect of Biot number on velocity and temperature profiles

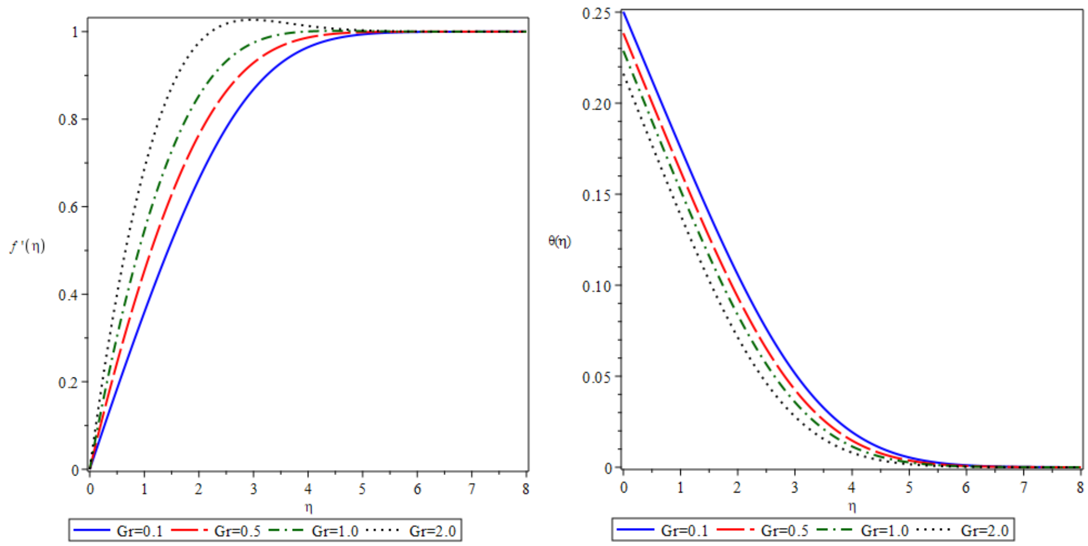

Figure 6: Effect of Grashof number on velocity and temperature profiles

Table 2: Validation of the present analysis through comparison with Jha and Samaila 2021 for $M=\delta=0$.

				Jha and Samaila 2021		Present		$\lvert\text{Error}\rvert$	
Bi_x	Gr_x	Pr	R	$-\theta'(0)$	$f''(0)$	$-\theta'(0)$	$f''(0)$	$-\theta'(0)$	$f''(0)$
0.1	0.1	0.72	0.1	0.07498	0.37525	0.07505	0.36887	0.00007	0.00638
1.0	0.1	0.72	0.1	0.22636	0.49997	0.22952	0.44238	0.00316	0.05759
10	0.1	0.72	0.1	0.27463	0.56019	0.28078	0.47054	0.00615	0.08965
0.1	0.5	0.72	0.1	0.07615	0.52239	0.07611	0.49721	0.00004	0.02518
0.1	1.0	0.72	0.1	0.07712	0.67398	0.07702	0.63230	0.00010	0.04168
0.1	0.1	2.0	0.1	0.08098	0.35648	0.08103	0.35370	0.00005	0.00278
0.1	0.1	7.0	0.1	0.08664	0.34375	0.08666	0.34280	0.00002	0.00095
0.1	0.1	0.72	0.5	0.07438	0.37688	0.07493	0.36908	0.00055	0.00780
0.1	0.1	0.72	1.0	0.07361	0.37896	0.07478	0.36937	0.00117	0.00959

Table 3: Effect of the various parameters for linear and nonlinear density variation with temperature.

					$(\delta=0)$			$(\delta=1)$		
Bi_x	Gr_x	Pr	R	M	$-\theta'(0)$	$f''(0)$	$\theta'(0)$	$-\theta'(0)$	$f''(0)$	$\theta'(0)$
0.1	0.1	0.72	0.1	0.5	0.07741	0.79013	0.76014	0.07742	0.79338	0.22575
1.0	0.1	0.72	0.1	0.5	0.24388	0.83602	0.75612	0.24536	0.87239	0.75464
10	0.1	0.72	0.1	0.5	0.29593	0.85526	0.97041	0.29962	0.91618	0.97004
0.1	**0.5**	0.72	0.1	0.5	0.07777	0.86487	0.22227	0.07783	0.87996	0.22173
0.1	**1.0**	0.72	0.1	0.5	0.07817	0.95325	0.21833	0.07826	0.98121	0.21742
0.1	0.1	**2.0**	0.1	0.5	0.08349	0.78228	0.16510	0.08349	0.78362	0.16505
0.1	0.1	**7.0**	0.1	0.5	0.08887	0.77655	0.11133	0.08887	0.77699	0.11132
0.1	0.1	0.72	**0.5**	0.5	0.07693	0.79067	0.23067	0.07695	0.79409	0.23053
0.1	0.1	0.72	**1.0**	0.5	0.07631	0.79138	0.23691	0.07633	0.23675	0.23675
0.1	0.1	0.72	0.1	**0.5**	0.07741	0.79013	0.22588	0.07742	0.79338	0.22575
0.1	0.1	0.72	0.1	**1.0**	0.07830	1.05894	0.21704	0.07830	1.06145	0.21696
0.1	0.1	0.72	0.1	**1.0**	0.07916	1.45582	0.20837	0.07917	1.45770	0.20833

4.0 CONCLUSION

This study developed the unified non-similarity framework for MHD free convection from a vertical plate that simultaneously incorporates a transverse magnetic field, nonlinear Rosseland thermal radiation, a nonlinear Boussinesq buoyancy term, and a convective surface boundary condition. The governing equations were solved at two levels of truncation using the RKF45 method with Newton-Raphson shooting, validated against the similarity solutions of Jha and Samaila (2021) to five decimal places, and shown to produce residuals two orders of magnitude below the prescribed integration tolerance across all parameter combinations tested. The principal scientific contribution is the quantification of coupling effects that prior studies treated in isolation: specifically, the demonstration that the Lorentz force and nonlinear buoyancy interact in a way that makes the choice of density-temperature model consequential for structural assessment but not for heat transfer prediction. A clear practical threshold emerges: the nonlinear density-temperature model is necessary when $Bi \geq 1.0$ or $Gr \geq 0.5$, where the linear approximation underestimates skin friction by up to 7.12%; below these values the simpler linear model is adequate.

The present framework rests on several simplifying assumptions that bound its direct applicability: the Rosseland approximation is valid only for optically thick media; viscous dissipation and Joule heating are neglected, which is appropriate when the Eckert number and magnetic dissipation parameter are small but limits the model at very high velocities or strong magnetic fields; the small magnetic Reynolds number assumption ($\mathrm{Re}_m \ll 1$) restricts applicability to moderately conducting fluids at engineering scales; and the Newtonian, constant-property, steady-flow idealisation excludes non-Newtonian behaviour, variable viscosity, and transient effects present in many practical systems. Future work relaxing these constraints, incorporating variable fluid properties, surface porosity, non-Newtonian rheology, or a full numerical treatment of the non-similar system further downstream, would broaden the practical reach of the present results.

5.0 LIMITATIONS AND FUTURE WORK

Like every theoretical study, the present work rests on a set of simplifying assumptions that define the boundaries of its findings. The fluid is treated as Newtonian with constant thermophysical properties, the Rosseland approximation is valid only for optically thick media, viscous dissipation and Joule heating are neglected, and the small magnetic Reynolds number assumption limits applicability to moderately conducting fluids. The plate is also assumed to be smooth, flat, and impermeable, which is an idealisation of most practical engineering surfaces. These assumptions were necessary to keep the problem analytically tractable and physically transparent, but they do leave room for meaningful extensions. Future studies could relax these constraints by incorporating variable fluid properties, non-Newtonian fluid behaviour, surface porosity, or more complete radiation transport models. Extending the present framework to curved or inclined geometries, hybrid nanofluid systems, or unsteady flow configurations would also broaden its practical applicability. The two-level truncation approach adopted here for the non-similarity solution works well near the leading edge but a full numerical treatment of the non-similar system further downstream would provide a more complete picture of the streamwise flow development and is a natural next step for future work.

REFERENCES

Ahmad, S., Ashraf, M., & Ali, K. (2020). Simulation of thermal radiation in a micropolar fluid flow through a porous medium between channel walls. Journal of Thermal Analysis and Calorimetry. https://doi.org/10.1007/s10973-020-09484-9

Aydin, O., & Kaya, A. (2009). MHD mixed convective heat transfer flow about an inclined plate. Heat and Mass Transfer, 46(1), 129–136. https://doi.org/10.1007/s00231-009-0551-4

Das, K., & Sarkar, A. (2016). Effect of melting on an MHD micropolar fluid flow toward a shrinking sheet with thermal radiation. Journal of Applied Mechanics and Technical Physics, 57(4), 681–689. https://doi.org/10.1134/S002189441604012X

Ghadikolaei, S. S., Hosseinzadeh, K., Yassari, M., Sadeghi, H., & Ganji, D. D. (2017). Boundary layer analysis of micropolar dusty fluid with TiO2 nanoparticles in a porous medium under the effect of magnetic field and thermal radiation over a stretching sheet. Journal of Molecular Liquids, 244, 374–389. https://doi.org/10.1016/j.molliq.2017.08.111

Gireesha, B. J., Umeshaiah, M., Prasannakumara, B. C., Shashikumar, N. S., & Archana, M. (2020). Impact of nonlinear thermal radiation on magnetohydrodynamic three dimensional boundary layer flow of Jeffrey nanofluid over a nonlinearly permeable stretching sheet. Physica A: Statistical Mechanics and Its Applications, 124051.

Jha, B. K., & Samaila, G. (2021). Nonlinear approximation for natural convection flow near a vertical plate with thermal radiation effect. Journal of Heat Transfer, 143(5), 054501. https://doi.org/10.1115/1.4050374

Kogawa, T., Shoji, E., Okajima, J., Komiya, A., & Maruyama, S. (2019). Experimental evaluation of thermal radiation effects on natural convection with a Rayleigh number of 10^8–10^9 using an interferometer. International Journal of Heat and Mass Transfer, 132, 1239–1249. https://doi.org/10.1016/j.ijheatmasstransfer.2018.11.162

Lopez, A., Ibanez, G., Pantoja, J., Moreira, J., & Lastres, O. (2017). Entropy generation analysis of MHD nanofluid flow in a porous vertical microchannel with nonlinear thermal radiation, slip flow and convective-radiative boundary conditions. International Journal of Heat and Mass Transfer, 107, 982–994.

Magyari, E., & Pantokratoras, A. (2011). Note on the effect of thermal radiation in the linearized Rosseland approximation on the heat transfer characteristics of various boundary layer flows. International Communications in Heat and Mass Transfer, 38(5), 554–556.

Makinde, O. D., & Ogulu, A. (2008). The effect of thermal radiation on the heat and mass transfer flow of a variable viscosity fluid past a vertical porous plate permeated by a transverse magnetic field. Chemical Engineering Communications, 195(12), 1575–1584. https://doi.org/10.1080/00986440802115549

Mikhailenko, S. A., Miroshnichenko, I. V., & Sheremet, M. A. (2020). Thermal radiation and natural convection in a large-scale enclosure heated from below: Building application. Building Simulation, 14, 681–691.

Mukhopadhyay, S., Bhattacharyya, K., & Layek, G. C. (2011). Steady boundary layer flow and heat transfer over a porous moving plate in presence of thermal radiation. International Journal of Heat and Mass Transfer, 54(13), 2751–2757. https://doi.org/10.1016/j.ijheatmasstransfer.2011.03.017

Qasem, S. A., Sivasankaran, S., Siri, Z., & Othman, W. A. M. (2020). Effect of thermal radiation on natural convection of a nanofluid in a square cavity with a solid body. Thermal Science, 24(1), 182–193.

Raju, R. S., Sudhakar, K., & Rangamma, M. (2013). The effects of thermal radiation and heat source on an unsteady MHD free convection flow past an infinite vertical plate with thermal diffusion and diffusion thermo. Journal of The Institution of Engineers (India): Series C, 94(2), 175–186.

Sangapatanam, S., Reddy, N., & Prasad, V. R. (2009). Thermal radiation effects on MHD free convection flow past an impulsively started vertical plate with variable surface temperature and concentration. Journal of Naval Architecture and Marine Engineering, 5(2). https://doi.org/10.3329/jname.v5i2.2695

Sheikholeslami, M., & Shehzad, S. A. (2017). Thermal radiation of ferrofluid in existence of Lorentz forces considering variable viscosity. International Journal of Heat and Mass Transfer, 109, 82–92. https://doi.org/10.1016/j.ijheatmasstransfer.2017.01.096

Singh, O., Kedare, S. B., & Singh, S. (2020). The validity of approximate boundary conditions for natural convection with thermal radiation in open cavities. Journal of Heat Transfer, 142(9).

Tian, X.-Y., Li, B.-W., & Zhang, J.-K. (2017). The effects of radiation optical properties on the unsteady 2D boundary layer MHD flow and heat transfer over a stretching plate. International Journal of Heat and Mass Transfer, 105, 109–123. https://doi.org/10.1016/j.ijheatmasstransfer.2016.09.060

Wang, S., Ai, Q., Zou, T., Sun, C., & Xie, M. (2020). Analysis of radiation effect on thermal conductivity measurement of semi-transparent materials based on transient plane source method. Applied Thermal Engineering, 181, 115457.

Zainal, N. A., Nazar, R., Naganthran, K., & Pop, I. (2020). MHD flow and heat transfer of hybrid nanofluid over a permeable moving surface in the presence of thermal radiation. International Journal of Numerical Methods for Heat & Fluid Flow, 31(3), 858–879.

Alzahrani, A. K., Ullah, M. Z., Alshomrani, A. S., & Gul, T. (2022). Entropy generation and Joule heating of MHD Casson nanofluid in a channel with nonlinear thermal radiation. Journal of Thermal Analysis and Calorimetry, 147, 7995–8007. https://doi.org/10.1007/s10973-021-10980-8

Algehyne, E. A., Alhusayni, Y. Y., Tassaddiq, A., Saeed, A., & Bilal, M. (2024). Nonlinear thermal radiation and MHD effects on ternary nanofluid flow over a stretching surface with heat source. Scientific Reports, 14, 3801. https://doi.org/10.1038/s41598-024-53038-2

Khan, U., Zaib, A., Ishak, A., Waini, I., Raizah, Z., Boonsatit, N., & Jirawattanapanit, A. (2022). Impact of nonlinear thermal radiation on the time-dependent flow of non-Newtonian nanoliquid over a permeable shrinking surface. Symmetry, 14(10), 2030. https://doi.org/10.3390/sym14102030

Saranya, S., Al-Mdallal, Q. M., & Animasaun, I. L. (2023). Shifted Legendre collocation analysis of time-dependent Casson fluids and Casson nanofluids flow induced by an exponentially elongated sheet with nonlinear thermal radiation. Nanoscale Advances, 5, 5640–5658. https://doi.org/10.1039/D3NA00108C

Waqas, H., Farooq, U., Liu, D., Abid, M., Imran, M., & Muhammad, T. (2023). Numerical investigation of MHD hybrid nanofluid flow with nonlinear thermal radiation and velocity slip over a rotating disk. Journal of Thermal Analysis and Calorimetry, 148, 2179–2195. https://doi.org/10.1007/s10973-022-11444-4

Yasmin, H., Giwa, S. O., Noor, S., & Sharifpur, M. (2023). Experimental exploration of hybrid nanofluids as energy-efficient fluids in solar and thermal energy storage applications. Nanomaterials, 13(2), 278. https://doi.org/10.3390/nano13020278

Zeeshan, A., Shehzad, N., Abbas, T., & Ellahi, R. (2022). Effects of radiative electro-magnetohydrodynamics diminishing internal energy of pressure-driven flow of titanium dioxide–water nanofluid due to entropy generation. Entropy, 24(2), 199. https://doi.org/10.3390/e24020199